Journal of Sound and Vibration 329 (2010) 277–288

Contents lists available at ScienceDirect

Journal of Sound and Vibration

journal homepage: www.elsevier.com/locate/jsvi

A model for an extensional mode resonator used as a frequency-adjustable vibration energy harvester

John M. Youngsman [a], Tim Luedeman [b], Dylan J. Morris [a,1], Michael J. Anderson [b], David F. Bahr [a,*]

[a] School of Mechanical and Materials Engineering, Washington State University, Pullman, WA 99164-2920, USA
[b] Department of Mechanical Engineering, University of Idaho, Moscow, ID 83844-0902, USA

ARTICLE INFO

Article history:
Received 16 March 2009
Received in revised form
23 July 2009
Accepted 10 September 2009
Handling Editor: D. J. Wagg
Available online 13 October 2009

ABSTRACT

In an effort to identify techniques for harvesting energy from ambient vibrations, a prototype device that utilizes stretching piezoelectric film to support a proof mass, with an adjustable support that allows the resonant frequency of the device to be easily altered, has been developed. This extensional mode resonator (XMR) device is described by a model developed in this paper that predicts the power that is harvested as a function of the frequency and amplitude of the external vibration, the elastic and piezoelectric materials properties, and the device geometry. The model provides design guidelines for the effects of device geometry and applied tension through an adjustable support that suggest a strong dependence on mechanical damping and a weak dependence on frequency, as opposed to a bending cantilever device. The model predictions are compared to experimental measures from a prototype device for frequencies between 120 and 180 Hz, and at accelerations between 0.1 and 10 m/s^2. Up to 9 mW is generated from a device with a mass of ~82 g, and over the range of frequencies tested the power harvested at 4 m/s^2 is between 3 and 4 mW.

1. Introduction

Improvements in wireless communication and sensing techniques, along with the reduction of power consumption in current microelectronics are driving demand for structural health monitoring systems. Although power consumption is low, battery life remains a critical factor in installation of distributed sensor networks. Because battery exchange requires considerable manpower, techniques are under investigation that can charge batteries or alternatively super capacitors as a means to extend the service life of installed networks. A larger concern is the installation that is either dangerous or no longer accessible for battery exchange. Solar generated power is ubiquitous, but is not a universal solution. A solution is required for installations that may not have or may not want solar exposure. Vibrations are available in many instances and can provide the critical energy input for the piezoelectric class of materials. Researchers are investigating vibration harvesting utilizing various self energizing techniques including electromagnetic in both a cantilever configuration [1–3] and single membrane form [4,5], and piezoelectric, principally as cantilevers [6,7]. A number of recent reviews discuss harvesting theory, techniques, and performance [8–12].

* Corresponding author.
E-mail address: dbahr@wsu.edu (.F. Bahr).
[1] Current address: Ceramics Division of the National Institutes of Standards and Technology, Gaithersburg MD 20899, USA.

0022-460X/$ - see front matter © 2009 Elsevier Ltd. All rights reserved.
doi:10.1016/j.jsv.2009.09.011

A critical issue with most resonating harvesters is their best performance occurs at a single or very narrow frequency range. Therefore, many devices must be designed for and limited to a known environment. Adjustable resonant tuning provides flexibility in a device and the opportunity to maximize power generation. Literature shows limited cases of resonant tuning and can be described as external electrical control [13,14], beam compression techniques [15–17], beam stiffness change through piezoelectric effect [15], beam stiffness change through magnetic field application [18], decoupling [19], cantilever arrays [20], or frequency rectification [21].

Frequency and acceleration measurements presented in [17,22] suggest a range of frequencies and magnitudes of interest for low level vibration harvesting. Frequencies range from 60 to 200 Hz with acceleration amplitudes on the order of 0.2–12 m/s^2. The measurements include an automobile engine compartment which garnered the highest frequency and acceleration measurements to measurements of a window subjected to traffic noise, a small microwave, a building's HVAC ductwork, a piece of industrial equipment, as well as others. Infrastructure monitoring falls into a different vibration spectrum than the typical machinery installation because buildings and bridges are so much larger. Literature reports spectra for small span bridges (including pedestrian walkways) in the 2–10 Hz range [23–26], large span bridges report typical resonant frequencies below 2 Hz [23,26], and a 27 story apartment building ranged between 0.4 and 3.3 Hz depending on the wind.

An issue with the cantilever design is the reduction in power output as the driving frequency increases. An accepted model predicting the maximum power of a cantilever harvester as postulated by a number of researchers [1,8,11,22,27] is written in Eq. (1) and a conditional form, Eq. (2) suggested by Morris et al. [28], is written

$$|\Pi| = \frac{m\zeta_E A^2}{4\omega\zeta_T^2} = \frac{b_E m^2 A^2}{2(b_E^2 + 2b_E b_M + b_M^2)} \tag{1,2}$$

where m is the mass, A is the acceleration amplitude, ζ_E and ζ_T are the electrical and total dimensionless damping coefficients, and b_E and b_M are the electrical and mechanical damping coefficients. The equation assumes that the natural frequency, ω_n, equals the driving frequency, ω. From Eq. (1) it is apparent that as the driving frequency increases, the power generated is reduced if the damping coefficients remain constant with frequency. The conditions of Eq. (2) assume the damping terms b_E and b_M remain constant with changes in device stiffness. This removes the dependence on frequency for electrical power generation.

The extensional mode resonator (XMR) [28] is constructed of piezoelectric films, in this case polyvinylidene fluoride (PVDF), that suspend a mass to a rigid frame. PVDF was chosen in this case for its availability and ease of use although the model does not preclude the use of any other piezoelectric material or composite capable of supporting a tensile load. However composite films present their own unique set of engineering challenges which would detract from the focus of this research. As the frame vibrates, the compliance of the films permits the mass to oscillate about a neutral axis which alternately stretches the films. The alternating strain cycle applied to the films generates electricity through the direct

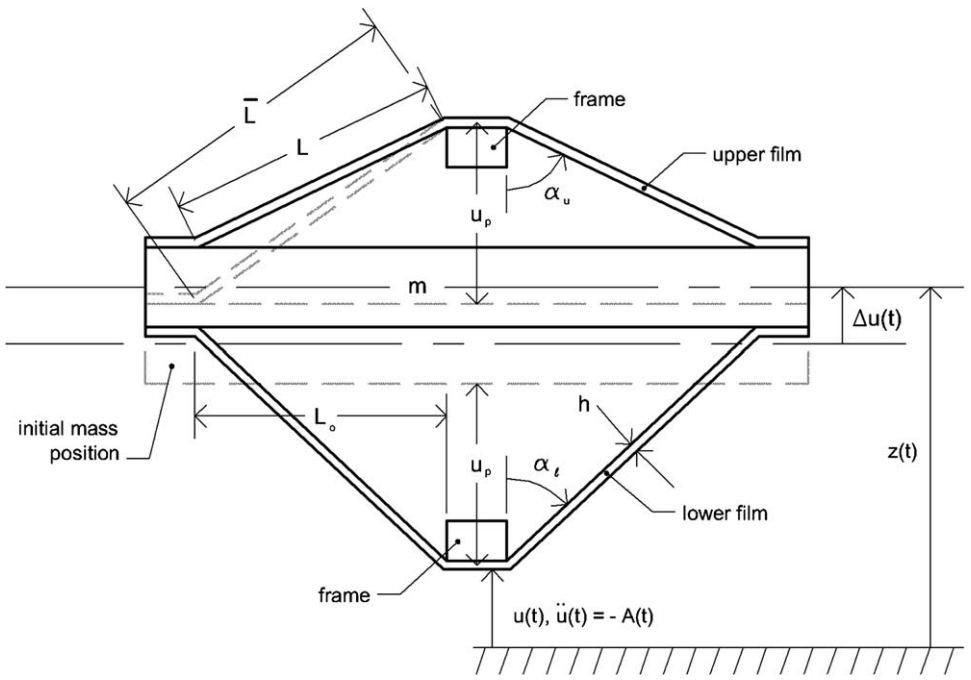

Fig. 1. Schematic for mechanical function of device.

piezoelectric effect. The unique geometry of the XMR permits simple adjustability of the resonant frequency through a change in stiffness rather than a change in mass. Initial experiments with the XMR device appear weakly dependant upon resonant frequency and more strongly affected by mechanical damping (b_M in Eq. (2)).

In addition to a very broad range of resonant frequency tunability, another advantage of the XMR design (Fig. 1) is the ability to utilize stretching rather than bending mode for generating the piezoelectric effect. In the case of the rectangular version in contrast to the circular version presented in Morris et al. [28], all strains are uniaxial and uniform. Because there is no strain gradient as in a cantilever [6], the entire active area of the films produce power effectively. The implications of geometry changes to the device stiffness and frequency are shown in the following model section followed by verification of the model with an experimental prototype device. The device size presented in this work is arbitrary and used as a means to develop and prove the model. Successful application of the model allows the design constraints to be optimized for a particular class of installations i.e. low frequency vibration (1–15 Hz) as would be present in a structural monitoring system or higher frequencies (60–120 Hz) more likely to be found in an industrial application.

2. Model

2.1. Dynamic model

Consider the schematic diagrams of the XMR shown in Figs. 1 and 2. They illustrate the mechanical and electrical function of the device. As shown in Fig. 1, the device consists of a moving mass m and adjustable frame. Four PVDF films, of unstretched length L_o, width w (into the plane of the figure), and thickness h are fixed to the moving mass and the central hub of the frame. The central hubs are moved vertically a distance u_p from the moving mass to preload the films and deform them to the dimension $\bar{L}$. The frame is moved at a specified inertial acceleration $\ddot{u}$, while the inertial displacement of the mass is z, and the displacement of the mass relative to the moving frame is Δu. While m executes relative movements Δu, the instantaneous length L of each film is $L = \bar{L} + \Delta L$, where ΔL is the stretch of each film caused by the movements Δu. In Fig. 2 the electrical function of the upper and lower films are shown symbolically. The top and bottom electrodes on the upper and lower sections are connected, so as to form the potentials ΔV_u and ΔV_l respectively. The polarity of the upper and lower films are indicated by "+" and "−", where the polarity is referenced to the free charge attracted to the electrode. The currents i_u and i_l flow into the top electrodes of the upper and lower films. A load resistor R_L is placed as shown to model harvesting of electrical energy, and the remaining electrodes will be connected such that i_u=i_l.

The objective is to develop a model that will predict the time-averaged power Π dissipated in a resistor placed across the electrodes of the XMR given a specified acceleration $\ddot{u}$. In what follows, Newton's second law will be derived for the vertical motion of m, and the electromechanical coupling of the PVDF film to a load resistor placed across the electrodes will be determined.

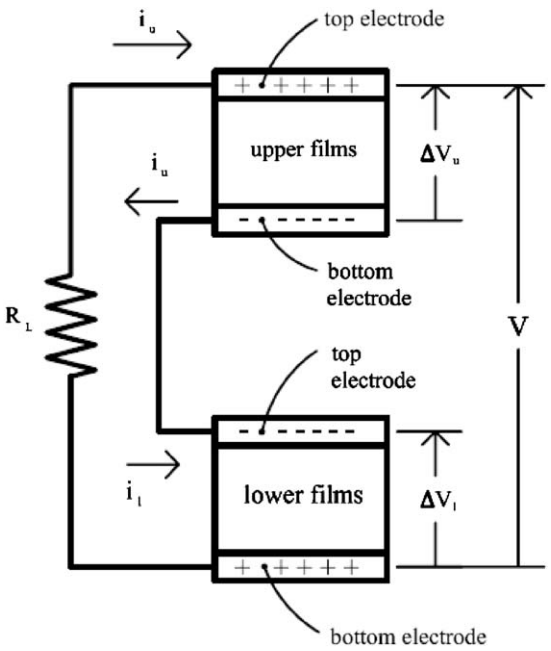

Fig. 2. Schematic for electrical function of device.

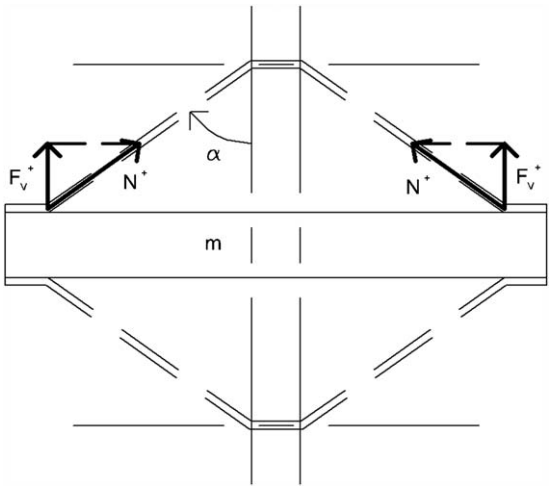

Fig. 3. Free-body diagram for mass m.

To derive the mechanical response of the device, consider the free-body diagram of the mass in the deflected condition shown in Fig. 3. Neglecting gravity, the only forces on the mass originate from the stretching of each PVDF film. Denote N as the axial force of a PVDF film on m, and F_v as the vertical component of the axial force N. Furthermore, the vertical reactions are subdivided in F_v^+ and F_v^- depending upon whether they originate from the upper or lower films respectively. The force F_v can be computed from $F_v=N\cos\alpha$, where the angle α is subscripted as α_u and α_l for the upper and lower films shown in Figs. 1 and 3. The axial force N can be computed from the constitutive equations for the film [29],

$$S_1 = -d_{31}E_3 + s_{11}^E T_1 \tag{3}$$

$$D_3 = \varepsilon_{33}^T E_3 - d_{31}T_1 \tag{4}$$

where S, T, E, and D are strain, stress, electric field and electric displacement; d_{31}, s_{11}^E, and ε_{33}^T are the piezoelectric coefficient, mechanical compliance and electric permittivity; the 1-direction is along the film axis and the 3-direction is in the film thickness direction. In Eqs. (3) and (4), the upper films are assumed to be oriented such that a release in tension associated with positive movements Δu of m cause a positive voltage at the top electrode, consistent with Fig. 2. Consequently, the piezoelectric coefficient d_{31} is taken to be negative. The constitutive model Eqs. (3) and (4) assumes that the stress in the 2-direction is zero (T_2=0), and that the films are free to contract in the 2-direction. This is a simplifying assumption in the model, and its quantitative effect will be neglected at this point in time. Given that $T_1=N/wh$ because a tension on an upper film is a force F_v in the opposite direction on m, $F_v=N\cos\alpha$, $S_1=\Delta L/L_o$, and $\Delta V = -\int_0^h E_3\,dz$, Eq. (3) can be rewritten for the upper and lower films as

$$F_v^+ = \frac{wh}{s_{11}^E}\frac{\Delta L}{L_o}\cos\alpha_u + \frac{d_{31}w}{s_{11}^E}\cos\alpha_u\Delta V_u, \quad F_v^- = \frac{wh}{s_{11}^E}\frac{\Delta L}{L_o}\cos\alpha_l - \frac{d_{31}w}{s_{11}^E}\cos\alpha_l\Delta V_l. \tag{5,6}$$

The component of the force F_v^- induced by the voltage ΔV_l on m from the lower film is negative because the polarity of the lower films are opposite that of the upper films. To obtain a linear model, it is assumed that Δu of m is small, and linearization of Eqs. (5) and (6) results in

$$F_v^+ = \frac{wh}{s_{11}^E}\frac{u_p}{L_o}\left\{1-\frac{1}{\left[1+\left(\frac{u_p}{L_o}\right)^2\right]^{1/2}}\right\} - \frac{wh}{s_{11}^E L_o}\left\{1-\frac{1}{\left[1+\left(\frac{u_p}{L_o}\right)^2\right]^{3/2}}\right\}\Delta u - \frac{d_{31}w}{s_{11}^E}\frac{u_p}{L_o}\frac{1}{\left[1+\left(\frac{u_p}{L_o}\right)^2\right]^{1/2}}\Delta V_u, \tag{7}$$

$$F_v^- = -\frac{wh}{s_{11}^E}\frac{u_p}{L_o}\left\{1-\frac{1}{\left[1+\left(\frac{u_p}{L_o}\right)^2\right]^{1/2}}\right\} - \frac{wh}{s_{11}^E L_o}\left\{1-\frac{1}{\left[1+\left(\frac{u_p}{L_o}\right)^2\right]^{3/2}}\right\}\Delta u - \frac{d_{31}w}{s_{11}^E}\frac{u_p}{L_o}\frac{1}{\left[1+\left(\frac{u_p}{L_o}\right)^2\right]^{1/2}}\Delta V_l. \tag{8}$$

The terms in Eqs. (7) and (8) above are caused by static extension of the films, displacements Δu caused by movement of the mass, and the voltages ΔV_u and ΔV_l induced across the electrodes of the upper and lower films. The total vertical force F on m from all four films then is

$$F = 2F_v^+ + 2F_v^- = -s\Delta u - \Psi\Delta V_u - \Psi\Delta V_l, \tag{9}$$

where

$$s = 4\frac{wh}{s_{11}^E L_o}\left\{1 - \frac{1}{\left[1+\left(\frac{u_p}{L_o}\right)^2\right]^{3/2}}\right\}, \Psi = 2\frac{d_{31}w}{s_{11}^E}\frac{u_p}{L_o}\frac{1}{\left[1+\left(\frac{u_p}{L_o}\right)^2\right]^{1/2}}. \tag{10,11}$$

Physically, s is a mechanical stiffness, and Ψ is a force coefficient with units of N/V. There are two components of s, one given by the extensional stiffness of the four films, and the other being a geometric dilution parameterized by the ratio u_p/L_o. Similarly, Ψ consists of a component that would be expected from extensional strains, and a geometric dilution. Newton's second law for the motion of the mass is

$$F - R_m(\dot{z} - \dot{u}) = m\ddot{z}, \tag{12}$$

where R_m is a coefficient of mechanical damping. Using the fact that $z=u+\Delta u$, letting $\ddot{u} = -A(t)$, and using Eq. (9) for F, Newton's law, Eq. (12), for m becomes

$$m\Delta\ddot{u} + R_m\Delta\dot{u} + s\Delta u + \Psi\Delta V_u + \Psi\Delta V_l = mA(t). \tag{13}$$

To derive the electrical response of the device, voltage–current laws are derived for the upper and lower films shown in Fig. 2. Starting with one of the upper films, elimination of the stress T_1 from Eqs. (3) and (4) gives

$$D_3 = \varepsilon_{33}^T\left(1 - \frac{d_{31}^2}{s_{11}^E\varepsilon_{33}^T}\right)E_3 - \frac{d_{31}}{s_{11}^E}S_1. \tag{14}$$

Upon integrating $\int_0^h(\,)\,dz$, using the fact that $\Delta V_u = -\int_0^h E_3\,dz$, $\partial D_3/\partial z = 0$ within the piezoelectric material, and $S_1 = \Delta L/L_o$, Eq. (14) becomes

$$hD_3 = -\varepsilon_{33}^T\left(1 - \frac{d_{31}^2}{s_{11}^E\varepsilon_{33}^T}\right)\Delta V_u - \frac{d_{31}}{s_{11}^E}h\frac{\Delta L}{L_o}. \tag{15}$$

Next, integrate over a volume of infinitesimal thickness enclosing the interface between the electrode and the piezoelectric film. This operation converts Eq. (15) to

$$wL_o hD_3 = -\varepsilon_{33}^T\left(1 - \frac{d_{31}^2}{s_{11}^E\varepsilon_{33}^T}\right)wL_o\Delta V_u + \frac{d_{31}}{s_{11}^E}wL_o h\frac{\Delta L}{L_o}. \tag{16}$$

To obtain a linear model for the upper films, $\Delta L/L_o$ is approximated for small motions Δu, the quantity wL_oD_3 is equated to the total free charge Q attracted to the electrode, and Eq. (16) is multiplied by two to reflect the fact that the two top and bottom electrodes are common. Additionally, it is assumed that charge caused by static deformation has been dissipated. One then obtains

$$-Q_u = -\overline{C}\Delta V_u + \Psi\Delta u, \tag{17}$$

where Q_u is the total free charge attracted to the top electrodes on the upper films and

$$\overline{C} = 2\frac{\varepsilon_{33}^T\left(1 - \frac{d_{31}^2}{s_{11}^E\varepsilon_{33}^T}\right)wL_o}{h}. \tag{18}$$

The derivation for the lower films is similar, only that the polarity orientation of the film is reversed, and positive movements of the mass Δu lead to extensional strains. For the lower films, the voltage–current law then is

$$-Q_l = -\overline{C}\Delta V_l + \Psi\Delta u. \tag{19}$$

As a final step, the circuit is completed by connecting the bottom electrode on the upper films to the top electrodes of the lower films. Then, $i_u=i_l$ and $V=\Delta V_u+\Delta V_l=-i_u R_L$, and the time derivative of the circuit equations for the upper and lower films are summed to obtain

$$C_o\dot{V} = -\frac{V}{R_L} + \Psi\Delta\dot{u}, \tag{20}$$

where

$$C_o = \frac{\overline{C}}{2} = \frac{\varepsilon_{33}^T\left(1-\dfrac{d_{31}^2}{s_{11}^E\varepsilon_{33}^T}\right)wL_o}{h}. \tag{21}$$

Eqs. (13) and (20) constitute a model for the device, where the acceleration of the frame $A(t)$ is the input, and there are two equations for the unknowns V and Δu.

2.2. Electric circuit analysis and energy harvesting capability

The model for the XMR device has a circuit analogy that is useful for analysis of power harvesting capability. Consider the circuit diagram shown in Fig. 4. With the definitions of voltage $mA(t)/\Psi$ and current $\Psi\Delta\dot{u}$, and the components $R=R_m/\Psi^2$, $L=m/\Psi^2$, and $C=\Psi^2/s$, the circuit shown in Fig. 4 can be verified to have the same governing equations as Eqs. (13) and (20). Furthermore, the natural frequency of the *RLC* circuit is

$$\omega_n = \frac{1}{\sqrt{LC}} = \sqrt{\frac{s}{m}} = \sqrt{\frac{1}{m}4\frac{wh}{s_{11}^E L_o}\left\{1-\frac{1}{\left[1+\left(\dfrac{u_p}{L_o}\right)^2\right]^{3/2}}\right\}}, \tag{22}$$

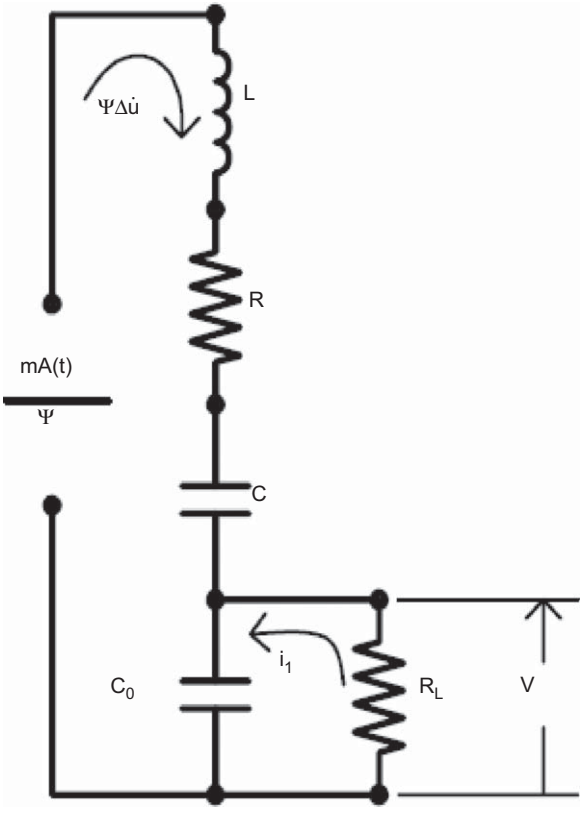

Fig. 4. Equivalent circuit diagram for device (Eqs. (13) and (20)).

and the quality factor Q is

$$Q = \frac{\sqrt{ms}}{R_m} = \frac{1}{R_m}\sqrt{m4\frac{wh}{s_{11}^E L_o}\left\{1 - \frac{1}{\left[1+\left(\frac{u_p}{L_o}\right)^2\right]^{3/2}}\right\}}. \tag{23}$$

Given a harmonic frame acceleration of amplitude A, it is necessary to specify the optimal frequency of operation and load resistance R_L. It has been shown [30,31] that in the limit of low damping, optimal power production is obtained at two frequencies, the resonance frequency given by (22) and the anti-resonance frequency. The optimal power production at the resonance and anti-resonance frequencies are equal. When damping becomes larger and exceeds a particular limit, called the bifurcation damping ratio [31] there is a single frequency for optimal power production. The value of the bifurcation damping ratio is determined by the effective electromechanical coupling factor of the device. Rather than compute an expression for power production in all three cases the scope was restricted to the case that damping is low, and power production was computed at ω_n. This choice was made because the device used in experimental measurements had low damping, and power production at the natural frequency also characterizes what might be expected for operation at the anti-resonance frequency. It is straightforward to compute Π at ω_n as

$$\Pi = \frac{1}{2}\frac{1}{R_L}\frac{1}{\left(\frac{R}{R_L}\right)^2 + 2\left(\frac{R}{R_L}\right) + (RC_o\omega_n)^2}\frac{m^2A^2}{\Psi^2}. \tag{24}$$

The optimal load resistance $R_{L,o}$ is found by maximizing Π. By differentiation of Π from Eq. (24), the optimal load resistance is found to be

$$R_{L,o} = \frac{R}{\sqrt{1+(RC_o\omega_n)^2}}. \tag{25}$$

Given an optimal load resistance specified by Eq. (25), the corresponding optimal time-averaged power dissipation Π_o from Eq. (24) will be

$$\Pi_o = \frac{1}{4R_m}\frac{1}{\sqrt{1+(RC_o\omega_n)^2}+1}m^2A^2. \tag{26}$$

3. Experiments

3.1. Prototype device

A prototype XMR was fabricated for experimental verification of the model. The active components of the device occupied a net volume of 21 cm^3. The total live mass of the device was 82.3 g. Commercially available PVDF film (Measurement Specialties, Inc.) was used as the piezoelectric element. Properties of the film provided by the manufacturer and other device constants are contained in Table 1.

3.2. Electrical impedance

Electrical impedance experiments were conducted with an Agilent 4294A precision impedance analyzer to determine the circuit parameters C_o, R, L, C and k^2. The electromechanical coupling coefficient k^2 is defined as the ratio of energy

Table 1
Device geometry constants and PVDF film properties.

m (g)	82.3
L_o (mm)	22
w (mm)	23.95
h (μm)	119
s_{11}^E (m^2/N)	3.65E–10
d_{31} (C/N)	–2.30E–11
ε_{33}^T (C/V/m)	1.10E–10
k_{31} (%)	1.15E–01

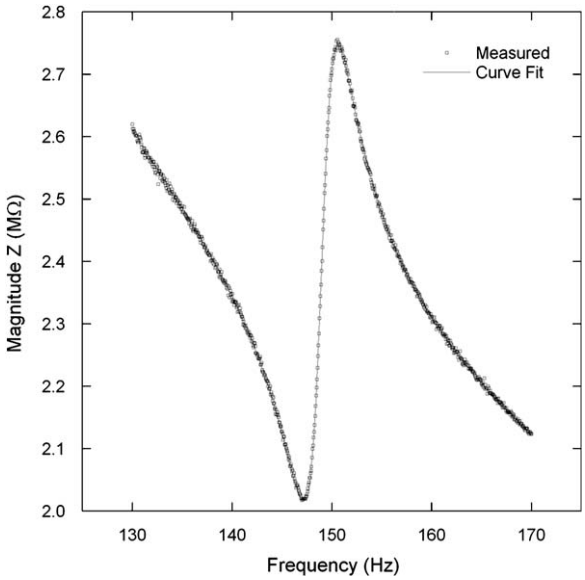

Fig. 5. Example measurement of electrical impedance and curve fit for circuit parameters R, L, C, C_o and k^2.

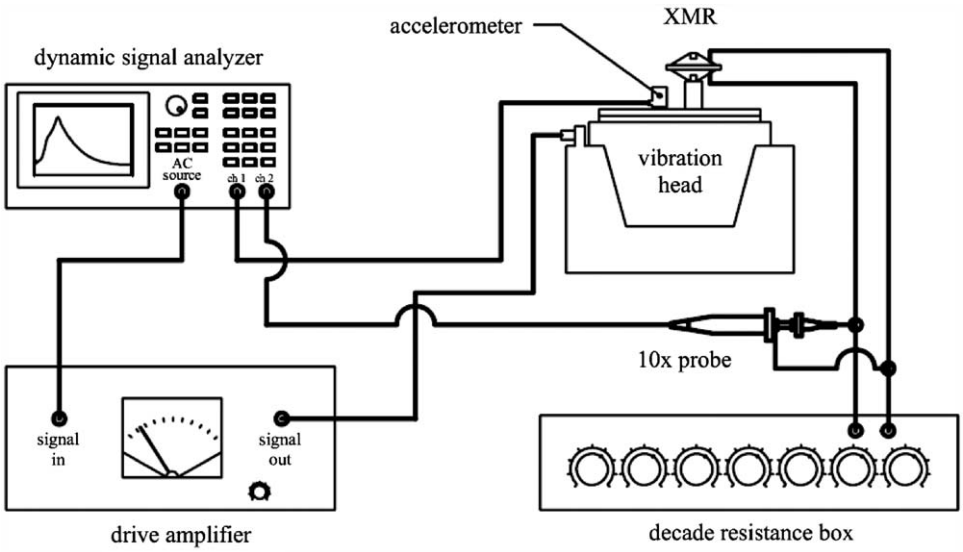

Fig. 6. Apparatus used to perform power output experiment from a controlled vibration source.

converted by the system divided by the energy input into the system. The impedance sweep data (Fig. 5) was curve fit using a least squares fit in which variables C_o, R, L, and C were allowed to change. The mechanical damping R_m was calculated using the measured R, Eq. (11) and the relationship $R_m=R\Psi^2$. Results from the impedance sweep were also used to find the optimal load resistance $R_{L,o}$ in order to achieve a matched impedance power experiment. The films were connected in series so that measurements captured the values of the device rather than the individual film elements. An electrical impedance measurement was conducted at each tension screw setting u_p, as the circuit parameters depended upon the device geometry as discussed in Section 2.

3.3. Mechanical vibration and power output

The schematic for the power measurement experiment is detailed in Fig. 6. The XMR device was mounted to a MB Electronics EA1250 vibration head driven with a MB Electronics 2120 amplifier. The input signal to the amplifier (both white noise and fixed sine) was generated by an Agilent 35670A Dynamic Signal Analyzer (DSA). Accelerations were

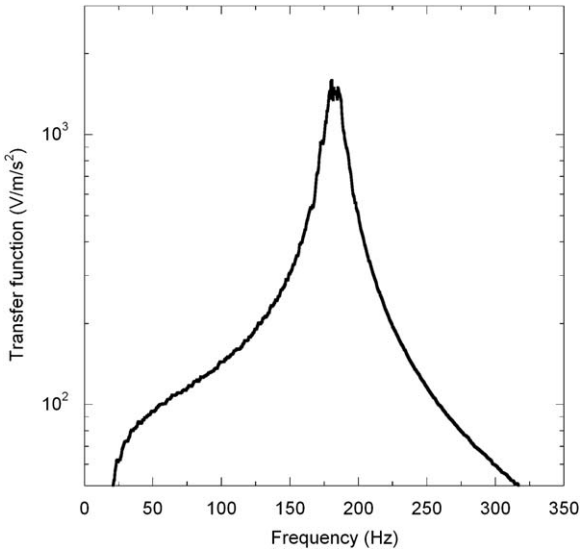

Fig. 7. Transfer function versus frequency of the XMR device. Peak indicates the resonant frequency of the oscillator.

measured with a Bruel & Kjaer Type 4395 accelerometer mounted to the vibration head. The impedance matched resistive load was provided by an AEMC BR07 decade resistance box.

The typical power measurement series was conducted by first exciting the XMR with white noise in order to determine the resonant frequency. In addition to providing the source signal, the DSA was used to capture the XMR and accelerometer output voltages and to plot the transfer function of mechanical excitation shown in Fig. 7. In this experiment the transfer function was defined as the output RMS open circuit voltage of the XMR divided by the acceleration. Open circuit condition refers to the absence of an electrical load across the film elements. The resonant frequency was identified by the maximum in the transfer function. Once the resonant frequency was found, the XMR was excited with a fixed sine signal at that resonant frequency at multiple accelerations. A feature of the DSA enables the use of measurement averaging (in this case, 50 measurements) to improve the resolution in V_{RMS} for each acceleration setting. Power was calculated from $P = V_{\mathrm{RMS}}^2/R_{\mathrm{L}}$. When all the desired measurements were collected, the XMR was tuned to a new resonant frequency by adjusting the tension screws. This step changed the u_{p} position and the initial tension in the films. For each position u_{p}, a new impedance measurement was conducted. Once the impedance measure was made, the power experiment was repeated.

4. Results

In this section, results of impedance and mechanical vibration measurements as described in Section 3 are presented. These measurements allow comparison of measured and theoretically predicted device parameters and power output. A discussion of properties of the device as predicted by the theoretical model follows in Section 4.1.

4.1. Impedance tests and device parameters

Table 2 provides a comparison of the XMR properties obtained in the impedance experiment with the values determined from the theoretical model. The model provides the fundamental values from geometry and materials properties to calculate the terms in Table 2 using the additional relationships $C = \Psi^2/s$, $L = \Psi^2/m$, $k^2 = C/(C + C_{\mathrm{o}})$, and $f_{\mathrm{n}} = \omega_{\mathrm{n}}/2\pi$. The geometric term u_{p} was selected to obtain nominal natural frequencies of f_{n}=120, 150, and 180 Hz, shown in Table 2.

Consider the measurements and predictions contained in Table 2 in which the XMR was configured to have a natural frequency of 120 Hz. Referring to the second column, a value of u_{p}=3.59 mm was selected. Because the value of L_{o} is known, and the assumption that the film elements are identical, it is straightforward to calculate a static strain of 1.32 percent in each film. Electrical impedance measurements gave the values shown in column two for C_{o}, R, L, C and k^2. Derived further from the impedance measurements was $\Psi = \sqrt{mL}$, $f_{\mathrm{n}} = 1/2\pi\sqrt{LC}$, and $s = \Psi^2/C$. Presently, the scope of the theoretical model does not include an *a priori* prediction of damping R_{m}. In the third column of Table 2 are theoretically predicted values of the device parameters using the expressions contained above and in Sections 2.1 and 2.2. The fourth column

Table 2
Configuration, impedance measurements, and theoretical predictions for nominal natural frequency of f_n=120, 150, and 180 Hz.

Parameter	120 Hz			150 Hz			180 Hz		
	Measured	Theoretical prediction	% Diff	Measured	Theoretical production	% Diff	Measured	Theoretical production	% Diff
u_p (mm)	3.59			4.62			5.67		
ε_o (%)	1.32			2.18			3.27		
C_o (pF)	461	479	−4	453	479	−5	458	479	−4
R (MΩ)	7.85			7.06			6.14		
L (kH)	473	349	36	308	214	44	212	145	46
C (pF)	3.81	4.29	−11	3.72	4.31	−14	3.76	4.33	−13
k^2 (%)	0.82	0.89	−8	0.81	0.89	−9	0.81	0.9	−10
f_n (Hz)	119	130	−8	149	166	−10	178	201	−11
R_m (Ns/m)	1.36			1.89			2.39		
Ψ (mN/V)	0.417	0.485	−14	0.517	0.62	−17	0.624	0.753	−17
s (kN/m)	45.7	54.9	−17	71.7	89.1	−20	103	131	−21
$R^*C_o^*\omega_n$	2.48			2.99			3.15		

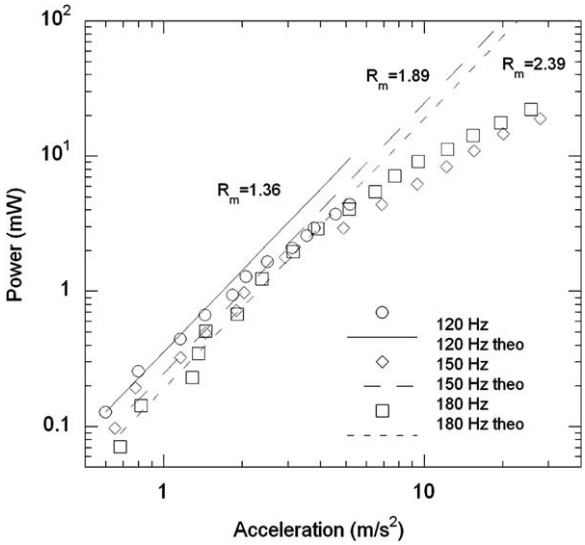

Fig. 8. Comparison of predicted power output for XMR configured with nominal natural frequencies of 120, 150, and 180 Hz.

shows the difference between the measured value and theoretical prediction expressed in percent. Columns 5–7 and 8–11 in Table 2 follow the same format as columns 2–4.

The fundamental properties of the XMR device can be divided into two categories. The first category, s, Ψ, C_o, and R_m are fundamental properties of the device. The second category of device parameters are those derived from s, Ψ, C_o, and R_m. These include effective electromechanical coupling factor k^2, and the product $RC_o\omega_n$. The product $RC_o\omega_n$ is discussed in Section 4.2 regarding power generation.

Referring to Table 2, it can be seen that the difference between theoretically predicted and measured values for s, Ψ, and C_o ranged from 4–21 percent. The predicted coupling factor and stiffness consistently exceeded their measured values by approximately 15–20 percent. The model prediction of natural frequency was within ~10 percent of the measured value. For several reasons, the agreement was thought to be reasonable for a first order predictive model. PVDF properties, s_{11}^E, d_{31}, and h used in the model prediction were nominal values reported by the manufacturer, and were not confirmed by independent measurement. It was unknown whether the manufacturer's specification for the permittivity is consistent with the tensor assumptions regarding ε_{33}^T in Eq. (4). There was no attempt to compensate these properties for the relatively large amount of static strain encountered during operation. For a first approximation, the model seems to be valuable for predicting s, Ψ, and C_o based only upon material properties and device geometry.

From Table 2, it was observed that the predicted and measured effective mechanical coupling coefficient k^2 was slightly less than 1 percent. At most, the predicted and measured value of k^2 differed by 10 percent.

4.2. Mechanical vibration and power output

A comparison of power output at the three nominal natural frequencies of 120, 150, and 180 Hz is shown in Fig. 8 corresponding to the configurations described in Table 2. To compute a predicted power output using Eq. (26) it was necessary to use a value for R_m obtained from impedance measurements of R, i.e., $R_m=R\Psi^2$. Multiple measurements of power were made for each device configuration to get an estimate of scatter. Maximum power outputs of 2.9, 4, and 4.4 mW were observed for acceleration amplitudes about 1/2 g and 9.4 mW and 9.5 mW at just under 1 g. The power output agreed very closely with theoretical predictions for small acceleration amplitudes, 1.3, 3, and 7 m/s^2, for nominal natural frequencies of f_n=120, 150, and 180 Hz respectively. At higher acceleration amplitudes, the predicted power output exceeded the measured values. This behavior would be expected, as the mathematical model assumed small motions of the proof mass. In a previous analysis, it was shown that the departure from a linearized analysis should occur at larger acceleration amplitudes as the ratio u_p/L_o increased [28]. The measurements shown in Fig. 8 are consistent with this analysis.

Referring to Table 2, the product $RC_o\omega_n$ for each configuration was in the range 2.48–3.19, and according to Eq. (26) would contribute little to changes in power output. It is apparent that the power output was not identical for the XMR configured for different natural frequencies, but the difference was attributed to a change in mechanical damping. Consequently, these measurements indicate that the power output changes little with the natural frequency of the device, but instead depends predominantly upon the amount of inherent mechanical damping in this device.

5. Conclusions

A tunable vibration harvesting device with an active volume of 21 cm^3 constructed of piezoelectric films supporting a mass of ~82 g with the ability to vary the resonant frequency was introduced. A model was developed that predicts the device performance from materials properties and device geometry. Results from the predictive model were confirmed with experimental measures with close correlation in the small deflection regime (small accelerations).

Model development included all the geometric and materials properties of the device. The model dynamics were derived from Newton's second law of motion, and the results were incorporated with the piezoelectric constitutive equations through an equivalent electrical circuit analysis to derive an equation for the power produced when the device is tuned to a given frequency and vibrated at a given acceleration. The power output was predicted and corroborated with experimental data for frequencies between 120 and 180 Hz and accelerations up to 1 g. Results at 1/2 g acceleration produced 3–4 mW at three different frequencies while producing up to 9 mW at just under 1 g acceleration. The model predictions indicated a dependence on both the frequency and mechanical damping. Both the model and the experimental measurements suggest that the damping has the greatest influence on performance.

The model provides a design tool for developing vibration harvesters that maximize power through a desired bandwidth. In the case where driving at resonance is deemed important, the environmental conditions can be measured and the model used to determine the geometry and dimensions of a device that will center on the resonant frequency and still allow a wide variation to either side of the center frequency in order to maximize power production upon installation to tune to a relatively wide range of local conditions. It should be noted that the design focuses on improving performance of a mechanical oscillator which dissipates generated power over a resistive load with no attempt to address the numerous electrical improvements suggested by literature which can be added to the system for additional improvement.

Acknowledgments

This work was financially supported through a subcontract from TPL Inc. of Albuquerque, NM under the SBIR program with the US Navy, Contract no. N68335-08-C-0098.

References

[1] S.P. Beeby, R.N. Torah, M.J. Tudor, P. Glynne-Jones, T.O. Donnell, C.R. Saha, S. Roy, A micro electromagnetic generator for vibration energy harvesting, *Journal of Micromechanics and Microengineering* (7) (2007) 1257.
[2] M. El-hami, P. Glynne-Jones, N.M. White, M. Hill, S. Beeby, E. James, A.D. Brown, J.N. Ross, Design and fabrication of a new vibration-based electromechanical power generator, *Sensors and Actuators A: Physical* 92 (1–3) (2001) 335.
[3] R. Amirtharajah, A.P. Chandrakasan, Self-powered signal processing using vibration-based power generation, *IEEE Journal of Solid-State Circuits* 33 (5) (1998) 687.
[4] C.B. Williams, C. Shearwood, M.A. Harradine, P.H. Mellor, T.S. Birch, R.B. Yates, Development of an electromagnetic micro-generator, *Circuits, Devices and Systems, IEE Proceedings* 148 (6) (2001) 337.
[5] N.N.H. Ching, W.J. Li, P.H.W. Leong, Z. Wen, H.Y. Wong, *A Laser-Micromachined Multi-Modal Resonating Power Transducer for Wireless Sensing Systems*, Elsevier Science BV, Munich, 2002.
[6] S. Roundy, E.S. Leland, J. Baker, E. Carleton, E. Reilly, E. Lai, B. Otis, J.M. Rabaey, P.K. Wright, V. Sundararajan, Improving power output for vibration-based energy scavengers, *IEEE Pervasive Computing* 4 (1) (2005) 28.
[7] M. Renaud, P. Fiorini, C. van Hoof, Optimization of a piezoelectric unimorph for shock and impact energy harvesting, *Smart Materials and Structures* (4) (2007) 1125.
[8] N.G. Stephen, On energy harvesting from ambient vibration, *Journal of Sound and Vibration* 293 (1–2) (2006) 409.

[9] S.P. Beeby, M.J. Tudor, N.M. White, Energy harvesting vibration sources for microsystems applications, *Measurement Science and Technology* 17 (12) (2006) 175–195.
[10] K. Nakano, S.J. Elliott, E. Rustighi, A unified approach to optimal conditions of power harvesting using electromagnetic and piezoelectric transducers, *Smart Materials and Structures* 16 (4) (2007) 948.
[11] S. Roundy, On the effectiveness of vibration-based energy harvesting, *Journal of Intelligent Material Systems and Structures* 16 (10) (2005) 809.
[12] P.D. Mitcheson, E.K. Reilly, T. Toh, P.K. Wright, E.M. Yeatman, Performance limits of the three MEMS inertial energy generator transduction types, *Journal of Micromechanics and Microengineering* (9) (2007) S211.
[13] G.K. Ottman, H.F. Hofmann, A.C. Bhatt, G.A. Lesieutre, Adaptive piezoelectric energy harvesting circuit for wireless remote power supply, *IEEE Transactions on Power Electronics* 17 (5) (2002) 669.
[14] W.J. Wu, Y.F. Chen, Y.Y. Chen, C.S. Wang, Y.H. Chen, *Smart Wireless Sensor Network Powered by Random Ambient Vibrations*, Institute of Electrical and Electronics Engineers Inc., Taipei, Taiwan, New York, NY, United States, 2007.
[15] S. Roundy, Y. Zhang, *Toward Self-tuning Adaptive Vibration Based Micro-Generators*, International Society for Optical Engineering, Sydney, Australia, Bellingham, WA, United States, 2005.
[16] E.S. Leland, P.K. Wright, Resonance tuning of piezoelectric vibration energy scavenging generators using compressive axial preload, *Smart Materials and Structures* (5) (2006) 1413.
[17] Y. Hu, H. Xue, H. Hu, A piezoelectric power harvester with adjustable frequency through axial preloads, *Smart Materials and Structures* 16 (5) (2007) 1961.
[18] V.R. Challa, M.G. Prasad, Y. Shi, F.T. Fisher, A vibration energy harvesting device with bidirectional resonance frequency tunability, *Smart Materials and Structures* (1) .
[19] J. Rastegar, C. Pereira, H.L. Nguyen, *Piezoelectric-Based Power Sources for Harvesting Energy from Platforms with Low Frequency Vibration*, International Society for Optical Engineering, United States, San Diego, CA, Bellingham, WA, United States, 2006.
[20] S.M. Shahruz, Design of mechanical band-pass filters with large frequency bands for energy scavenging, *Mechatronics* 16 (9) (2006) 523.
[21] R.M. Tieck, G.P. Carman, D.G. Enoch Lee, *Electrical Energy Harvesting Using a Mechanical Rectification Approach*, American Society of Mechanical Engineers, United States, Chicago, IL, New York, NY, United States, 2006.
[22] S. Roundy, P.K. Wright, J. Rabaey, A study of low level vibrations as a power source for wireless sensor nodes, *Computer Communications* 26 (11) (2003) 1131.
[23] G. Rossi, R. Marsili, V. Gusella, M. Gioffre, Comparison between accelerometer and laser vibrometer to measure traffic excited vibrations on bridges, *Shock and Vibration* 9 (1–2) (2002) 11.
[24] C.W. Lin, Y.B. Yang, Use of a passing vehicle to scan the fundamental bridge frequencies: an experimental verification, *Engineering Structures* 27 (13) (2005) 1865.
[25] M.J. Glanville, K.C.S. Kwok, R.O. Denoon, Full-scale damping measurements of structures in Australia, *Journal of Wind Engineering and Industrial Aerodynamics* 59 (2–3) (1996) 349.
[26] M. Yoshimura, Q. Wu, K. Takahashi, S. Nakamura, K. Furukawa, Vibration analysis of the Second Saikai Bridge—a concrete filled tubular (CFT) arch bridge, *Journal of Sound and Vibration* 290 (1–2) (2006) 388.
[27] C.B. Williams, R.B. Yates, Analysis of a micro-electric generator for microsystems, *Sensors and Actuators, A: Physical* 52 (1–3 pt 1) (1996) 8.
[28] D.J. Morris, J.M. Youngsman, M.J. Anderson, D.F. Bahr, A resonant-frequency tunable, extensional mode piezoelectric vibration harvesting mechanism, *Smart Materials and Structures* 17 (2008).
[29] G. Kino, *Acoustic Waves: Devices Imaging and Analog Signal Processing*, Prentice-Hall, Englewood Cliffs, NJ, 1987, p. 601.
[30] N.E. DuToit, B.L. Wardle, Experimental verification of models for microfabricated piezoelectric vibration energy harvesters, *AIAA Journal* 45 (5) (2007) 1126.
[31] J.M. Renno, M.F. Daqaq, D.J. Inman, On the optimal energy harvesting from a vibration source, *Journal of Sound and Vibration* 320 (1–2) (2009) 386.